eNeuro

Research Article: New Research | Disorders of the Nervous System

Traumatic brain injury diminishes feedforward activation of parvalbumin-expressing interneurons in the dentate gyrus

https://doi.org/10.1523/ENEURO.0195-19.2020

Cite as: eNeuro 2020; 10.1523/ENEURO.0195-19.2020

Received: 21 May 2019
Revised: 14 September 2020
Accepted: 20 September 2020

Manuscript Title: Traumatic brain injury diminishes feedforward activation of parvalbumin-expressing interneurons in the dentate gyrus

Abbreviated Title: TBI reduces activation of dentate gyrus interneurons

Authors: Kaitlin A. Folweiler,[1,2,3] Guoxiang Xiong,[1,2] Kaitlin M. Best, [1,2] Hannah E. Metheny,[1,2] Gabriel Nah,[1,2] Akiva S. Cohen[1,2,3]

Affiliations: [1]Department of Anesthesiology and Critical Care Medicine, Children's Hospital of Philadelphia, Philadelphia, PA 19104. [2]Department of Anesthesiology, Perelman School of Medicine, University of Pennsylvania, Philadelphia, PA 19104. [3]Neuroscience Graduate Group, University of Pennsylvania, Philadelphia, PA 19104

Author Contributions: K.F. and A.C. designed research, K.F., G.X., K.B., H.M., G.N., A.C. performed research, K.F., G.N. and A.C. analyzed data, K.F. wrote the paper.

Correspondence can be directed to:

Akiva S. Cohen, PhD
816-H Abramson Research Center
Children's Hospital of Philadelphia
3615 Civic Center Blvd. Philadelphia, PA 19104
Email: cohena@email.chop.edu

Number of Figures: 8
Number of Tables: 2
Number of Multimedia: 0
Number of words for Abstract: 192
Number of words for Significance Statement: 100
Number of words for Introduction: 311
Number of words for Discussion: 1527
Acknowledgements: The authors would like to thank Dr. Eric Marsh of Children's Hospital of Philadelphia for gift of transgenic mice.
Conflict of Interest: The authors report no conflict of interest.
Funding Sources: A.S. C. received support from NIH-NICHD R37 HD059288 and a grant from the Pennsylvania Department of Health

Abstract

Traumatic brain injury (TBI) is associated with aberrant network hyperexcitability in the dentate gyrus. $GABA_A$ergic parvalbumin-expressing interneurons (PV-INs) in the dentate gyrus regulate network excitability with strong, perisomatic inhibition, though the post-traumatic effects on PV-IN function after TBI are not well understood. In this study, we investigated physiological alterations in PV-INs one week after mild lateral fluid percussion injury (LFPI) in mice. PV-IN cell loss was observed in the dentate hilus after LFPI, with surviving PV-INs showing no change in intrinsic membrane properties. Whole-cell voltage clamp recordings in PV-INs revealed alterations in both excitatory and inhibitory postsynaptic currents (EPSCs/IPSCs). Evoked EPSCs in PV-INs from perforant path electrical stimulation were diminished after injury but could be recovered with application of a $GABA_A$-receptor antagonist. Furthermore, current-clamp recordings using minimal perforant path stimulation demonstrated a decrease in evoked PV-IN action potentials after LFPI, which could be restored by blocking $GABA_A$ergic inhibition. Together, these findings suggest that injury alters synaptic input onto PV-INs, resulting in a net inhibitory effect that reduces feedforward PV-IN activation in the dentate gyrus. Decreased PV-IN activation suggests a potential mechanism of dentate gyrus network hyperexcitability contributing to hippocampal dysfunction after TBI.

Significance Statement

Traumatic brain injury (TBI) damages the hippocampus and causes long-lasting memory deficits. After TBI, the dentate gyrus, a crucial regulator of cortical input to the hippocampus, undergoes a dysfunctional net increase in excitation, though the circuit mechanisms underlying this network excitatory-inhibitory (E/I) imbalance are unclear. In this study, we found that TBI alters synaptic inputs onto an inhibitory interneuron population (PV-INs) in the dentate gyrus which results in

the decreased firing activity of these neurons due to a net inhibitory influence. The inhibition of PV-INs demonstrates a potential mechanism contributing to dentate gyrus network hyperexcitability and hippocampal dysfunction after TBI.

Introduction

Fast-spiking, parvalbumin-expressing GABAergic interneurons (PV-INs) are powerful regulators of excitability in neural networks and play an important role in mediating hippocampal-dependent cognitive behaviors (Armstrong and Soltesz, 2012; Freund and Buzsáki, 1996; Fuchs et al., 2007; Hu et al., 2014; Nitz and McNaughton, 2004). In the hippocampus, PV-INs contribute to the ability of the dentate gyrus sub-region to act as a filter or gate of incoming sensory information from the cortex by providing strong feedforward inhibition onto granule cells (Coulter and Carlson, 2007). In combination with the low intrinsic membrane excitability of granule cells, PV-IN GABAergic inhibition contributes to sparse granule cell action potential firing under normal conditions (Ewell and Jones, 2010; Kraushaar and Jonas, 2000).

After traumatic brain injury (TBI), the dentate gyrus experiences network hyperexcitability (Lowenstein et al., 1992; Santhakumar et al., 2000; Toth et al., 1997; Witgen et al., 2005). Granule cells no longer sparsely fire action potentials, and evoked extracellular burst discharges are increased in the granule cell layer *in vivo* (Lowenstein et al., 1992). This shift toward a hyperexcitable network state leads to a break down in the physiological filtering function of the dentate gyrus and is associated with spatial memory impairments (Folweiler et al., 2018).

One week after TBI, the frequency of miniature inhibitory postsynaptic currents (mIPSCs) is reduced in granule cells, suggesting that a loss of synaptic inhibition is contributing to granule cell hyperexcitability (Toth et al., 1997; Witgen et al., 2005). While previous studies have looked at other populations of dentate inhibitory interneurons after TBI (Butler et al., 2017; Hunt et al., 2011), the potential role of PV-INs in dentate network hyperexcitability after injury has yet to be examined. In order to understand the effects of TBI on PV-IN inhibition, we investigated the intrinsic membrane properties and synaptic inputs of PV-INs in the dentate gyrus one week after mild lateral fluid percussion injury (LFPI).

Materials and Methods

Mice

All experiments were performed in accordance with protocols approved by our institution's Institutional Animal Care and Use Committee and the guidelines established by the U.S. Public Health Service's Guide for the Care and Use of Laboratory Animals. Experiments were designed to minimize the number of animals required and those used were cared for, handled, and medicated as appropriate to minimize their suffering. To visually identify PV-INs, PV^{CRE} transgenic mice, expressing Cre-recombinase in parvalbumin-expressing neurons ($129P2^{Pvalbtm1(cre)Arbr}$/J; Jackson Laboratory, Bar Harbor, ME, USA. RRID:IMSR_JAX:008069) were crossed with tdTomato reporter mice (129S6-Gt(ROSA)26Sor$^{m14(CAG-tdTomato)Hze}$/J; Jackson Laboratory, RRID:IMSR_JAX:007908) to generate PV^{CRE};*tdTomato*$^{+/-}$ (i.e., PV-Tomato) transgenic animals which express tdTomato fluorescence in parvalbumin-positive cells. All experiments were performed on 6-8-week-old male and female PV-Tomato mice. The primary purpose of using both male and female mice was to utilize all transgenic animals that were bred

for experiments with the secondary aim of reducing sex bias by favoring one sex over another (Will et al., 2017). The number of male and female mice in each group is listed by experiment in Table 1.

Surgical procedures

Animals were anesthetized with a mixture of ketamine (2.6mg/kg) and xylazine (0.16 mg/kg) via intraperitoneal injection. Once fully anesthetized, animals were placed in a stereotaxic frame (Stoetling, Wood Dale, IL, USA), the scalp was incised and pulled away to fully expose the right parietal bone. An ultra-thin Teflon disk, with the outer diameter equal to the inner diameter of a trephine was glued to the skull with Vetbond (3M, St. Paul, MN, USA) between lambda and bregma sutures, and between the sagittal suture and the lateral ridge over the right hemisphere. Guided by the Teflon disk, a trephine was used to perform a 3-mm diameter craniectomy over the right parietal area. Following craniectomy, a Luer-lock needle hub (3-mm inner diameter) was secured above the skull opening with superglue (Loctite, Düsseldorf, Germany) and dental acrylic, filled with saline and capped. Lastly, animals were removed from stereotaxis, placed on a heating pad until fully recovered from anesthesia, and then returned to their respective home cage.

Lateral fluid percussion injury (LFPI)

Twenty-four hours following craniectomy, animals were placed under isoflurane anesthesia (2% oxygen in 500ml/min) in a chamber and respiration was visually monitored until animals reached a surgical plane of anesthesia (one respiration per 2 s). At this point, animals were removed from isoflurane, the needle hub was refilled with saline and connected to the fluid percussion injury

device (Department of Biomedical Engineering, Virginia Commonwealth University, Richmond, VA, USA) via high-pressure tubing. The animal was placed onto a heating pad on its left side and upon resumption of normal breathing pattern but before sensitivity to stimulation, the injury was induced by a 20-millisecond pulse of saline onto the intact dura. The pressure transduced onto the dura was monitored with an oscilloscope, with injury severity ranging between 1.4 and 1.6 atmospheres. Immediately after injury, the hub was removed from the skull and the animal was placed in a supine position to assess righting reflex. After righting, the animal was subjected to inhaled isoflurane to suture the scalp. Animals were allowed to recover on a heating pad until mobile, at which point they were returned to their home cage. Sham animals underwent all surgical procedures including attachment to the FPI device with exclusion of the actual fluid pulse.

PV-IN cell counting

To show changes (if any) in number of PV-Tomato interneurons resulted from TBI, sham and LFPI mice (7 d post-injury) were deeply anesthetized with 5% chloral hydrate and perfused with 15 ml of saline followed by 50 ml of paraformaldehyde (4% in phosphate buffer, pH 7.4; Sigma-Aldrich, St. Louis, MO, USA). The brains were removed and post-fixed in the fixative for 90 min. Vibratome slices were cut at 50 µm in thickness with a VT 1000S (Leica, Buffalo Grove, IL) and collected in serial from a fixed brain. The slices were treated with 0.3% Triton X-100 for 1 hour at room temperature (RT) and then counterstained with Hoechst, a DNA dye to stain nuclei of all cells in a slice. Hoechst staining (blue) made it easier to outline the structure and boundary of the hippocampus when counting PV-Tomato cells (red) in dentate gyrus (Figure 1). Fluorescent images were acquired with an Olympus BX-51 microscope at 10X magnification.

All tdTomato-positive neurons in the dentate gyrus ipsilateral to the injury site were quantified using modified stereology with the optical fractionator method in which every sixth section through the rostral/caudal extent of the dorsal hippocampus (bregma -1.00 to -2.75 mm) was examined (Eisch et al., 2000; Mouton, 2002; West et al., 1991). Cells were scored as tdTomato–positive if tdTomato labeling in the soma was more intense than background (Lim et al., 2013). Since counting of cells was conducted on every sixth section of the hippocampus, the number of cells in each anatomical region was multiplied by six to obtain the reported estimate of the total number of cells per region. Cell anatomical location was considered by both dentate blade (suprapyramidal or infrapyramidal) and cellular layer, including molecular layer, granule cell layer, subgranular zone, and hilus. TdTomato-positive cells in the hilus but within one soma length (20-30 μm) of the granule cell layer were considered in the subgranular zone (Figure 1).

Immunofluorescent staining

To show if PV-Tomato cells in DG from the transgenic mouse did express PV, we also performed PV immunofluorescent staining on brain slices containing the hippocampus from sham and injured mice. The slices were treated with 0.3% Triton X-100 and blocked with a mixture of 1% BSA and 5% normal goat serum, 60 min respectively. They were then incubated with a monoclonal antibody against PV (1:1000; Sigma-Aldrich, St. Louis, MO), 60 min at RT and overnight at 4°C. Visualization was done by incubating the slices with Alexa Fluora 488-conjugated goat anti-mouse IgG for 75 min at RT. The immunostained slices were mounted on pre-cleaned slide glass and coverslipped with aqueous mounting medium. In a stained brain slice, PV immunostained cells showed green and PV-Tomato cells red (Figure 2). PV-Tomato

cells expressing PV should be identified as yellowish to brown, depending upon the intensity of tdTomato (red).

Timm staining

To examine whether mossy fiber spouting existed in the hippocampus, Timm staining was performed according to a protocol reported previously (Van der Zee et al., 1995). Mice were perfused with 15 ml of saline followed by 50 ml of sodium sulfide perfusion medium containing 8.9 g of $Na_2S{\cdot}9H_2O$, 10.9 g of sucrose and 1.19 g of $Na_2PO4{\cdot}H_2O$ dissolved in 100 ml of deionized water (DW). The brains were removed and post-fixed in the same perfusion medium for 3 hours at RT. Untreated vibratome slices (50 µm in thickness) were mounted on gelatin-coated slide glass and air-dried overnight. They were then incubated in dark for 60 min with a mixture containing 6 volume of gum arabic (50 g/100 ml), 3 volume of hydroquinone (5.67 g/100 ml) and 1 volume of citric acid -sodium citrate buffer (25.5 g and 23.5 g respectively in a total of 100 ml). For each 100 ml of the incubation solution, 0.5 ml of silver nitrate stock solution (1.7g $AgNO_3$ /10 ml) was added. Staining was stopped by brief rinse in DW 3 times. The slices (on glass) were then dehydrated and cleared before coverslipped with Permount. Brightfield microscope was used to observe positive Timm staining. Mossy fiber sprouting was defined as Timm-stained axonal collaterals (black) present in the molecular layer of dentate gyrus.

Electrophysiology

All recordings were made 5–9 days after LFPI or sham surgery. Mice were anesthetized with isoflurane, and the brains were quickly and carefully removed, then placed into ice-cold

oxygenated (95% O_2/5% CO_2) sucrose artificial cerebral spinal fluid (ACSF) containing (in millimolar): sucrose 202, KCl 3, NaH_2PO_4 1.25, $NaHCO_3$ 26, glucose 10, $MgCl_2$ 1, and $CaCl_2$ 2. Coronal slices 350 µM thick containing the dorsal hippocampus were cut on a VT1200S vibratome (Leica Microsystems Inc., Buffalo Grove, IL, USA) and transferred to 33–37°C normal ACSF containing (in millimolar): NaCl 130, KCl 3, NaH_2PO_4 1.25, $NaHCO_3$ 26, glucose 10, $MgCl_2$ 1, $CaCl_2$ 2, for at least 45 minutes.

Extracellular field recordings

Electrodes for recordings field excitatory post-synaptic potentials (fEPSPs) were fabricated from borosilicate glass (World Precision Instruments, Sarasota, FL, USA, #1B150F-4), pulled to a tip resistance of 2–6 MΩ and filled with aCSF. fEPSPs were recorded from an electrode placed in the suprapyramidal molecular layer. Stimulating electrodes were non-concentric bipolar (World Precision Instruments, Sarasota, FL, USA, #ME12206) and placed at the apex of the molecular layer. Electrical stimuli were 100 µs in duration. Field potential input–output relationships were recorded in response to increasing stimulating intensities (20–400 µA stimulation, 20 µA increments, 8 second inter-stimulus interval) from each slice. For each stimulation intensity, recordings were averaged from three trials, and the field EPSP (fEPSP) slope was calculated for the first linear portion of the fEPSP (i.e., monosynaptic response). Recordings were obtained with an Axoclamp 900A amplifier and pClamp10 data acquisition software (Molecular Devices, Sunnyvale, CA, USA; RRID:SCR_011323), filtered at 2 kHz. Field potential data was analyzed using pClamp10 software and custom-written scripts in MATLAB R2012b (MathWorks, Natick, MA, USA).

221

222 *Whole-cell patch clamp recordings*

223 Patch electrodes with resistances of 4–7 MΩ were pulled from borosilicate glass (World
224 Precision Instruments, Sarasota, FL, USA). Series resistance was monitored throughout the
225 experiment and recordings were discontinued if series resistance exceeded 25 MΩ at any point.
226 Series resistance was compensated for at 70-80% compensation. All recordings were made using
227 a Multiclamp 700B (Molecular Devices, Palo Alto, CA, USA) sampled at 20 kHz, filtered at
228 2 kHz. Electrophysiological data were analyzed using Clampfit 10 and MATLAB software.
229 Synaptic events were determined via the Template Search algorithm in Clampfit 10.

230

231 PV-INs were visually identified by fluorescent tdTomato expression in cells within the granule
232 cell layer, subgranular zone, or hilar subregion within 100 μm of the hilar-granule cell layer
233 interface. In order to confirm that tdTomato-expressing neurons also had a fast-spiking
234 electrophysiological signature, experiments began with a series of depolarizing current steps.
235 Any neurons that failed to demonstrate non-accommodating trains of action potentials with a
236 maximum spiking frequency greater than 30Hz (Kawaguchi and Kubota, 1997) in response to
237 depolarizing current injections, or that demonstrated baseline instability, were excluded from
238 further analysis. All whole-cell recordings were performed in one cell per brain slice and are
239 reported as n cells per n mice in each group.

240

241 Resting membrane potential was computed as the average voltage in the first 2 seconds
242 immediately after whole-cell configuration was achieved. All other intrinsic excitability
243 measures were computed from current clamp recordings consisting of a series of ten 500 ms

current steps, from −100 to 250 pA in 50 pA increments. Constant holding current was applied to maintain the neuron at −65 mV before and after current steps. Action potential threshold was computed by taking dV/dt of the voltage trace at 175 pA in the intrinsic excitability experiments and then averaging the corresponding voltage values for the first 10 spikes where dV/dt exceeded 30 mV/ms (Howard et al., 2007). Input resistance was determined from the steady-state voltage response for the four initial current steps (-100 pA to 50 pA). Action potential frequency and corresponding inter-spike-intervals were calculated for all current steps resulting in action potential firing.

For whole-cell patch-clamp recording of excitatory postsynaptic currents and intrinsic excitability measures electrode internal solution contained (in millimolar): K-Gluconate 140, EGTA 5, HEPES 10, $MgCl_2$ 1, $CaCl_2$ 1, KOH 3, Mg-ATP 2, and was titrated to a final pH of 7.1–7.3 with KOH and osmolality of 290-300 mOsm. Bicuculline methiodide (30 µM, BMI, Abcam, Cambridge, UK) was added before voltage clamp recordings, and tetrodotoxin (0.4 µM, TTX, Abcam) was added to isolate miniature events (mEPSCs). Neurons were voltage-clamped at −65 mV for all EPSC voltage-clamp experiments. Liquid junction potential of 16.9 mV (calculated in Clampex) was corrected for in all data reported from these experiments. For whole-cell patch-clamp recording of inhibitory currents, internal solution contained (in millimolar): Cs-gluconate 140, NaCl 1, EGTA 5, $MgCl_2$ 1, $CaCl_2$ 1, KOH 3, Mg-ATP 2, and was titrated to a final pH of 7.2-7.3 with CsOH and an osmolality of 290-300 mOsm. APV (50 µM, Abcam), CNQX (6 µM, Abcam), and QX-314 (5 mM, Abcam) were added before voltage clamp recordings, and TTX (0.4 µM) was added to isolate mIPSCs. Liquid junction potential of 2.0 mV was corrected for in all data reported from these experiments. Neurons were voltage-clamped at

0 mV for all voltage clamp experiments of inhibitory currents. The slice chamber temperature for all recordings was set to 29-31°C.

To record perforant path-evoked excitatory postsynaptic currents (eEPSCs), a non-concentric bipolar placed in at the apex of the molecular layer was used to stimulate afferent axons onto patch-clamped PV-INs held at -65 mV in voltage-clamp. Evoked potentials were recorded in response to electrical stimulation from 10–100 μA in 10 μA incremental steps). Three input-output eEPSCs were recorded and averaged from each cell. Extracellular fEPSPs were simultaneously recorded in the molecular layer during evoked voltage-clamp and current-clamp experiments and eEPSC for each recorded cell were normalized to the fiber volley amplitude of the slice. As for fEPSP recordings, the first linear, monosynaptic portion of the eEPSC was used to calculate the slope. For current-clamp experiments, an electrode was placed in the perforant path at the apex of the molecular layer. Minimal current stimulation was adjusted to find the lowest current intensity parameter that could elicit at least one action potential in a series of 20 stimulations. Once the minimal stimulation current intensity was set, three series of 20 stimulations (12 second interstimulus interval) were administered and the number of stimulus-evoked action potentials (APs) for each series was recorded and reported as a percentage of the total number of stimulations in that series (20 stimulations per series). Throughout current-clamp recordings, a slow injection of current was given to maintain a membrane potential of -65 mV. Stimulus-evoked APs were recorded in normal aCSF baseline and then in the presence of 100 nM picrotoxin (PCTX). Cells were recorded in voltage clamp after PCTX wash-in to confirm that IPSCs were eliminated.

Statistical procedures

A priori power calculations using β=0.8 were performed using G*Power statistical software to determine the minimum sample size required for each experiment (Faul et al. 2007). Electrophysiological and cell count data were analyzed using pClamp 10 and GraphPad Prism 7.0 software (GraphPad Software, San Diego, CA, USA; RRID:SCR_002798). Data distributions were initially tested for normality using both Shapiro-Wilk and Agostino-Pearson tests. Statistics were performed using either unpaired Student's t-test, or two-way repeated measures ANOVA with Sidak's multiple comparison test unless use of another test is indicated (Table 2). In experiments with small sample sizes, effect sizes were reported using Glass's *delta*. Cumulative distribution functions of synaptic event properties were constructed by randomly sampling the same number of events (n = 75) from each cell. The Kolmogorov-Smirnov (K-S) test was used for statistical comparison of synaptic current measurements. *N* refers to number of cells and number of animals as described in the results of each experiment. Statistical significance was set at $p < 0.05$.

Results

Parvalbumin immunostaining confirms td-Tomato expression in PV-positive cells.

Cre-tdTomato colocalization was confirmed in a subset of animals (sham n = 3, LFPI n = 4). Cells were classified as having tdTomato and PV-immunostaining colocalization, PV-immunostaining only, or tdTomato only (Figure 2). There was no difference in the number of cells where tdTomato and PV-immunostaining overlapped (Sham: mean ± SD = 78.4% ± 5.5% of total cells; LFPI: mean ± SD = 78.9% ±11.9% of total cells, p = 0.949, Table 2-a). The majority of cells that did not colocalize tdTomato and PV+, were PV+ only (Sham = 18.5% ±

5.9%; LFPI = 13.8 ± 9.7% total cells) and there was no difference in the number of PV+ only cells between sham and LFPI animals (p = 0.47, Table 2-1b). The occurrence of tdTomato only cells was extremely rare (Sham = 3.0% ± 5.3%; LFPI = 0.99% ± 1.4%, p = 0.56, Table 2-1c) and did not differ significantly between the injury groups. While tdTomato was not expressed in all PV+ cells, this analysis shows that almost all tdTomato cells were PV+ and counting tdTomato cells provides a good estimate for PV cell prevalence.

Mild LFPI induces loss of hilar tdTomato-expressing neurons

Previous studies have found fewer hilar GABA-expressing neurons, including PV-INs, one week after fluid percussion injury, however these studies utilized a more moderate (2.0-2.2 atm) pressure impact than that implemented in this study (Hunt et al., 2011; Lowenstein et al., 1992; Santhakumar et al., 2000; Toth et al., 1997). Additionally, some studies have observed post-traumatic mossy fiber sprouting (MFS) in the dentate gyrus molecular layer (Hunt et al., 2011). To test if hilar PV-IN cell loss occurred in our mild (1.4-1.6 atm) LFPI model, we counted the number of tdTomato-expressing cells in the dorsal dentate gyrus ipsilateral to the injury site in sham (n=8 50-µm sections per mouse, 8 mice; Figure 3A) and LFPI (n=8 50-µm sections per mouse, 9 mice; Figure 3B). At one week after injury, the total number of dentate PV-INs appeared to trend downward but did not result in a statistically significant change after injury (Sham: mean ± SEM = 650 ± 65 cells; LFPI mean ± SEM = 485 ± 54, p = 0.067; Figure 3C, Table 2-2a). However, there were significantly less tdTomato-positive cells in the hilus (Sham: mean ± SEM = 104 ± 14 cells; LFPI mean ± SEM = 61 ± 10, p = 0.028; Figure 3D, Table 2-2b). PV-IN cell counts remained unchanged in the subgranular zone, granule cell layer, molecular layer, suprapyramidal blade, and infrapyramidal blade when respectively counted

(Table 2-2c-g). There were no septotemporal differences in PV-IN cell counts (Two-way ANOVA, $F(1,87) = 0.87$, $p = 0.35$, Table 2-2f). Furthermore, to examine whether mossy fiber sprouting (MFS) was present in our LFPI model seven days following injury, we performed Timm staining to label mossy fiber projections (i.e., granule axons and axon terminals) in the dentate gyrus ($n = 10$ animals in each group). No Timm stained fibers were observed in the molecular layer of LFPI (Figure 3E-F) or sham animals at seven days post-injury, suggesting that MFS was not present at the time point observed after injury in our LFPI model.

Dentate network hyperexcitability persists in PV-Tomato mouse line

To ensure that injury alters dentate excitability in our transgenic PV-Tomato mice, input/output (I/O) curves were generated by electrically stimulating perforant path fibers (stimulation intensity range: 20-400 μA, 20 μA increments, 100 μs duration) and recording extracellular field potentials in the molecular layer one week after LFPI or sham surgery ($n = 6$ mice in each group, 3 slices per animal) with transgenic animals (Figure 4A). In brain slices from sham animals, fEPSP slope increased almost linearly as perforant path stimulation intensity increased (Figure 4B). Slices from LFPI animals demonstrated significantly larger fEPSP slopes with increasing stimulation intensity compared with sham (repeated-measures ANOVA, $F(19,190) = 14.34$; $p < 0.0001$, Table 2-3a). This injury-induced shift in the I/O curve demonstrates that dentate post-traumatic hyperexcitability is present in the transgenic mouse line used for further experiments in this study.

PV-IN intrinsic membrane properties are unaffected by injury

Neuronal intrinsic membrane properties, dictated predominantly by membrane proteins and their subsequent activity, play a significant role in a neuron's propensity to fire action potentials. After experimental TBI, alterations in intrinsic properties have been observed in dentate glutamatergic neurons (Gupta et al., 2012; Howard et al., 2007). To investigate the intrinsic properties of dentate PV-INs, we performed whole-cell patch clamp recordings one week after LFPI or sham surgery (Figure 4C-G, n = 10 cells in each group, 1 cell per animal). Passive properties such as membrane input resistance (Figure 4D; sham: 92.2 ± 6.3 MΩ; LFPI: 88.6 ± 7.5 MΩ; p = 0.71, Table 2-3b), and resting membrane potential (Figure 4E; mean ± SEM = -65.3 ± 1.4 mV in sham and -62.9 ± 1.2 mV in LFPI; p = 0.22, Table 2-3c), were not significantly different between cells from sham and LFPI groups. Additionally, PV-IN active firing properties were not affected by injury. PV-INs from sham animals had on average an action potential threshold of -29.8 ± 1.0 mV, while cells from LFPI animals had an average firing threshold of -32.7 ± 2.1 mV (Figure 4F; p = 0.23, Table 2-3d). Action potential firing frequency in response to depolarizing current steps (400 – 550 nA, 50 nA steps) was unaltered by injury (Figure 4C and 2G; sham: n = 8 cells, LFPI: n = 7 cells; repeated measures ANOVA: $F(1,13) = 0.42$; p = 0.53, Table 2-3e). Lastly, action potential half-width, was not significantly different between sham and injured groups (Sham: mean ± SEM = 0.74 ± 0.06 ms; LFPI: mean ± SEM = 0.69 ± 0.04 ms; p = 0.55, Table 2-3f). These findings suggest that there is no net change in either passive or active intrinsic membrane properties of PV-INs after injury.

Excitatory synaptic inputs onto PV-INs exhibit post-traumatic changes

To examine whether excitatory synaptic input to dentate PV-INs was altered after LFPI, whole-cell voltage-clamp recordings of miniature excitatory postsynaptic currents (mEPSCs) were

obtained from sham and LFPI brain slices (sham: n = 7 cells, 5 animals; LFPI: n = 6 cells, 6 animals). Representative recordings for each group are shown in Figure 5A. The frequency of mEPSCs was increased in PV-INs after injury as observed by a decrease in inter-event intervals (Sham: median (IQR) = 281 (640.2) ms; LFPI: median (IQR) = 164 (436.9) ms, $p < 0.0001$, K-S test; Figure 5B, Table 2-4a). Additionally, mEPSC event amplitudes were larger after LFPI (Sham: median (IQR) = 30.8 (19.4) pA; LFPI: median (IQR) = 33.7 (19.9) pA, $p = 0.006$, K-S test; Figure 5C; Table 2-4b) and had faster rise kinetics (rise τ, Sham: median (IQR) = 0.41 (0.70) ms; LFPI: median (IQR) = 0.32 (0.66) ms, $p = 0.004$, K-S test; Table 2-4c). No change in mEPSC decay kinetics was observed (decay τ, Sham: median (IQR) = 0.99 (2.28) ms, LFPI: median (IQR) = 0.83 (1.92) ms, $p = 0.20$, K-S test; Table 2-4d).

PV-INs receive less feed-forward excitation from the perforant path after injury

Since local dentate glutamatergic neurons have demonstrated increased activity after experimental TBI (Gupta et al., 2012; Lowenstein et al., 1992; Santhakumar et al., 2000), it is likely that a decrease in action potential-mediated excitatory drive is coming from perforant path synapses. To test the effect of injury on feed-forward excitation of PV-INs, we examined the I/O relationship of evoked EPSCs (eEPSCs) by electrical stimulation of the perforant path at incremental stimulus intensities (Figure 6A *top row*; 10-100 μA). While the slope of perforant path eEPSCs was not significantly different between PV-INs from sham (n = 12 cells, 6 animals) and injured (n = 11 cells, 6 animals. Figure 6B *left*; repeated measures ANOVA, $F(1, 13) = 0.1825$, $p = 0.68$; Table 2-5a), there was a decrease in eEPSC amplitude (Figure 6B *middle*; repeated measures ANOVA, amplitude: $F(1,22) = 4.715$, $p = 0.041$, Table 2-5b) and charge transfer with increasing stimulus intensities (Figure 6B *right*; $F(1,21) = 5.426$, $p = 0.029$, Table

2-5c). BMI was then washed in to block local GABAergic inhibition onto cells in sham and LFPI slices, respectively, and evoked synaptic current properties were re-examined (Figure 6A *bottom row*). In the absence of inhibition, LFPI eEPSC I/O curves were similar to sham (Figure 6C *left*; eEPSC slope: $F(1,10) = 0.005$, $p = 0.94$; Figure 6C *middle;* eEPSC amplitude: $F(1, 10) = 0.86$, $p = 0.37$; Figure 6C *right;* eEPSC charge transfer: $F(1, 10) = 0.95$, $p = 0.35$, Table 2-5d-f). There was no difference in the passive intrinsic properties of PV-INs used in current clamp experiments (Resting membrane potential, sham: mean ± SEM = -64.5 ± 2.6 mV; LFPI: mean ± SEM = -61.0 ± 2.5 mV; whole-cell capacitance, sham: mean ± SEM = 43.4 ± 6.8 pF; LFPI: mean ± SEM = 43.7 ± 6.5 pF). These data suggest that diminished feed-forward excitatory synaptic transmission from the perforant path onto dentate PV-INs is due to GABAergic inhibition after injury.

Increased synaptic inhibitory input onto PV-INs after LFPI

To understand how brain injury affects inhibitory synaptic transmission onto dentate PV-INs, we next recorded miniature action potential-independent inhibitory events (mIPSCs; Figure 7A, sham: n = 6 cells/animals, LFPI: n = 7 cells/animals). We observed an increase in the amplitude of mIPSCs after injury (Figure 7B; Sham: median (IQR) = 18.3 (11.6) pA, LFPI: median (IQR) = 19.6 (16.8) pA, $p = 0.0003$, K-S test, Table 2-6a). Rise kinetics were significantly faster in LFPI PV-INs (rise τ; Sham: median (IQR) = 0.73 (0.71) ms; LFPI: median (IQR) = 0.63 (0.75) ms, $p = 0.0079$, K-S test; Table 2-6b). Injury did not affect mIPSC event frequency however, as the inter-event interval between events was not significantly different between PV-INs from sham and injured slices (Figure 7C; Sham: median (IQR) = 268 (468.3) ms; LFPI: median (IQR) = (412.3) 237 pA, $p = 0.26$, K-S test; Table 2-6c). Miniature IPSC decay tau also remained intact

after injury (Sham: median (IQR) = 5.6 (8.4) ms; LFPI: median (IQR) = 7.8 (9.7) ms, p = 0.86, K-S test; Table 2-6d). These results demonstrate that PV-INs receive larger AP-independent GABAergic events after LFPI, but that the frequency or ionotropic $GABA_A$-receptor kinetics is unchanged.

Decrease in PV-IN action potentials is due to net GABAergic inhibition

The results of the whole-cell patch clamp recordings indicate that there are changes in both excitatory and inhibitory synaptic inputs onto PV-INs after brain injury. These alterations affect the synaptic balance of PV-INs and influence the cells' ability to fire an action potential by depolarizing or hyperpolarizing the membrane potential. To understand the net effect of post-traumatic synaptic alterations on the feed-forward activation of PV-IN neurons, we performed a series of perforant path minimal stimulation experiments and counted the number of PV-INs evoked action potentials recorded in current-clamp (Figure 8A; n = 5 cells, 5 animals, in each group). Prior to current clamp recording, resting membrane potential and whole-cell capacitance were measured in each cell. Neither resting membrane potential (Sham: mean ± SEM = -64.5 ± 2.67 mV; LFPI: mean ± SEM = -61.0 ± 2.48 mV, p = 0.37) nor whole-cell capacitance (Sham: mean ± SEM = 43.4 ± 6.81 pF; LFPI: mean ± SEM = 43.8 ± 6.48 mV, p = 0.64, Table 2-7a-b) differed between groups. In normal aCSF solution, PV-INs from LFPI slices had a significantly lower percentage of evoked action potentials than cells from sham slices (Figure 8B *black circles*; % evoked APs, Sham: mean ± SEM = 57.8% ± 6.3; LFPI: mean ± SEM = 12.0% ± 4.0, p = 0.0008, Welch's unpaired t-test, Glass's d = 3.6; Table 2-7c;). There was no difference between the baseline stimulation levels of sham and LFPI groups (Sham: mean ± SEM = 44 ± 21.6 µA; LFPI: mean ± SEM = 50 ± 21.7 µA, two-sample t-test t = -0.19, p = 0.85). Next, 100

nM PCTX was bath applied to remove $GABA_A$-mediated inhibition from PV-INs. PCTX significantly increased the percentage of evoked action potentials in both sham (Sham pre-PCTX: mean ± SEM = 57.8% ± 6.3; Sham post-PCTX: mean ± SEM = 92.6% ± 6.2, p = 0.0004, paired t-test, Table 2-7d) and LFPI PV-INs (LFPI pre-PCTX: mean ± SEM = 12.0% ± 4.0; LFPI post-PCTX: mean ± SEM = 78.6% ± 10.6, p = 0.0034, paired t-test, Table 2-7e). After PCTX application, there was no difference in the percentage of PV-IN evoked action potentials in sham and LFPI groups (Figure 8B *gray squares*; % evoked APs, sham: mean ± SEM = 92.6% ± 6.2, LFPI: mean ± SEM = 78.6% ± 10.6, p = 0.29, Welch's unpaired t-test, Glass's d = 1.13; Table 2-7f). These findings demonstrate that feed-forward activation of PV-INs is compromised by network inhibition.

Discussion

In the dentate gyrus, GABAergic basket cells and axo-axonic cells (i.e., PV-INs) are important drivers of feedforward inhibition onto granule cells (Ewell and Jones, 2010; Kraushaar and Jonas, 2000). Previous work has shown that feedforward inhibitory control of dentate granule cell firing is compromised after LFPI (Toth et al., 1997; Witgen et al., 2005). In seeking to identify potential cellular sources of granule cell disinhibition, this study is the first to demonstrate altered excitability of dentate PV-INs following experimental TBI. First, we showed that mild LFPI induced a loss of PV-INs in the hilus, recapitulating hilar interneuron loss observed in previous studies using moderate LFPI (Lowenstein et al., 1992; Santhakumar et al., 2000; Toth et al., 1997; Witgen et al., 2005). While surviving PV-INs have normal intrinsic membrane properties, excitatory and inhibitory synaptic currents are respectively shifted after injury. Furthermore, the data reveal that cortical feedforward activation of PV-INs is diminished

due to a net inhibitory effect and lead to decreased evoked PV-IN firing. Together, our findings demonstrate a mechanism of reduced network inhibition contributing to dentate gyrus and hippocampal dysfunction following TBI.

The observed hilar PV-IN cell loss demonstrates that interneurons in this subregion are vulnerable to cell death in a milder model of LFPI (1.4-1.6 atm). A recent study of mild LFPI in rats also found a non-specific decrease in PV-INs seven days post-injury (Zhang et al., 2018). The steady number of PV-INs in the subgranular zone and granule cell layers supports findings by Toth and colleagues, who proposed that laminar cell density plays a role in injury-induced neuronal loss, and with loose cell packing in the hilus leading to cell death susceptibility (Toth et al., 1997). An advantage of cell counts in the PV-Tomato transgenic mice used is that fluorescence protein expression is controlled by the *CAG* promoter and therefore was not directly linked to PV-expression after injury. Therefore, it is unlikely that the decrease in tdTomato-positive cell bodies is due to reduced PV protein expression or immunoreactivity (Nichols et al., 2018). However, we cannot rule out that brain injury may negatively affect CAG promotor activation and interfere with fluorescent protein expression.

When we examined the intrinsic membrane excitability of PV-INs, we observed no differences in passive or active properties following injury. Other dentate cells types have also been shown to retain their intrinsic properties, suggesting that the composition of membrane leak and voltage-gated channels are not overtly altered by LFPI (Howard et al., 2007; Santhakumar et al., 2001, 2000). This could reflect homeostatic compensation by opposing modifications of intrinsic currents, as was previously observed in mossy cells after injury (Howard et al., 2007). This is

496 opposed to the transient depolarization found in dentate interneurons due to diminished Na^+/K^+
497 ATPase activity during the early acute post-injury period (i.e., four days after FPI; Ross and
498 Soltesz, 2000). Therefore, at seven days after injury, homeostatic mechanisms may have
499 recalibrated PV-IN membrane properties. Further inspection of isolated ionic currents may be
500 required to rule out the contribution of compensatory cellular processes of maintaining PV-IN
501 intrinsic excitability and to better understand the dynamicity of cellular properties during the
502 post-traumatic period.
503
504 While the intrinsic properties of PV-INs remained intact, changes in both excitatory and
505 inhibitory synaptic currents reflected post-traumatic circuit-level alterations. On the excitatory
506 side, miniature EPSCs had larger amplitude events, suggesting a larger postsynaptic response
507 (e.g., increased insertion of receptors into the membrane) or larger presynaptic quantal size. The
508 kinetics of mEPSCs were unchanged after injury. Several factors contribute to changes in rise
509 and decay kinetics, including dendritic filtering, glutamate clearance, and receptor subunit
510 composition. The lack of differences in the kinetics of miniature EPSCs between sham and LFPI
511 groups suggests that factors like glutamate clearance and dendritic filtering may not play a
512 prominent role in integration of excitatory post-synaptic currents by PV-INs (Diamond and Jahr,
513 1997; Magee and Cook, 2000; Williams and Mitchell, 2008). Furthermore, PV-INs in LFPI
514 animals demonstrated increased mEPSC frequency. More frequent mEPSC events may reflect in
515 increased in basal excitatory transmission mediated by changes in release probability or
516 increased presynaptic activity, the latter which has support from previous studies that local
517 dentate glutamatergic neurons are more excitable after injury (Gupta et al., 2012; Santhakumar et

al., 2000). This suggests that basal excitatory synaptic transmission onto PV-INs after LFPI may be a consequence of increased local glutamatergic activity in the dentate gyrus network.

On the inhibitory side, mIPSCs demonstrated larger amplitudes but did not alter their frequency of occurrence, suggesting either an increase in postsynaptic response such as more $GABA_A$-receptors inserted into the postsynaptic membrane, or the presynaptic packaging of larger GABA quantal sizes. Specifically, enhanced inhibitory events may indicate an increase in tonic GABA-receptor mediated currents, as have been shown in dentate PV-INs after status epilepticus and granule cells in a controlled cortical impact TBI model (Mtchedlishvili et al., 2010; Yu et al., 2013). Additionally, mIPSCs in LFPI animals had faster rise kinetics than in sham animals. The kinetics of IPSCs at GABAergic synapses are determined by the properties of their postsynaptic receptors. Differences in IPSC kinetics may suggest alterations in the activation or recruitment of $GABA_A$-receptors with different subunit compositions. Phasic inhibition results are mediated by activation of synaptically located, α1 and γ2 subunit-containing postsynaptic receptors by saturating concentrations of GABA. Tonic inhibition results from activation of extrasynaptic $GABA_A$-receptors containing α4 and δ subunit-containing by low concentrations of ambient GABA (Rossi and Hamann, 1998; Stell and Mody, 2002; Mody and Pearce, 2004). Extrasynaptic $GABA_A$-receptors are slow to desensitize while their synaptic counterparts rapidly desensitize. Therefore, it is possible that faster mIPSC rise times suggest alterations in postsynaptic receptor subunit composition.

After LFPI, perforant path-evoked EPSCs were smaller than sham controls, but returned to sham levels when GABAergic inhibition was blocked by BMI wash-in. No change in eEPSC slopes

indicated that the activation of the evoked response was not affected, but the amplitude and overall charge transfer are decreased because of an enhanced inhibitory tone onto PV-INs. Minimal stimulation experiments further demonstrated that net augmentation of GABAergic inhibition decreased PV-INs evoked APs in response to entorhinal afferent input. This finding has major implications for predicting the activity of PV-INs in the post-traumatic dentate gyrus. It also provides additional evidence that injury-induced granule cell disinhibition may be attributed to decreased activation of feedforward GABAergic sources. While the results of our study do not provide a direct link between altered PV-IN firing and diminished GABAergic synaptic transmission onto granule cells, they do demonstrate network alterations in synaptic transmission that affect the functional activation of PV-INs. The post-traumatic decrease in mIPSC frequency onto granule cells seen previously suggests that there are fewer inhibitory synapses onto granule cells, potentially including loss of hilar PV-IN connections (Soltesz et al., 1995; Toth et al., 1997).

At the circuit level, loss of perisomatic inhibitory control of dentate granule cells is likely to disrupt the gating function of the dentate gyrus after TBI. Additionally, decreased feedforward recruitment of PV-INs could have cognitive consequences. Fuchs and colleagues have previously demonstrated that loss of PV-IN recruitment lead to impaired performance on hippocampal-dependent behavioral task in mice when excitatory drive onto PV-INs was knocked out (Fuchs et al., 2007). Therefore, alterations in PV-IN activation and network recruitment could have profound effects on cognitive processes and potentially underlie hippocampal-dependent cognitive deficits experienced by TBI patients. Future studies would benefit from investigating potential changes in the properties of PV-IN synapses onto granule cells, as previous work

564 suggests that these synapses may have higher failure rates and smaller pools of readily releasable
565 vesicles in a model of dentate network hyperexcitability (Zhang and Buckmaster, 2009).
566
567 There are several limitations of this study. It is important to note that perisomatic inhibitory
568 control of dentate granule cells is provided by nonoverlapping populations of PV+ *and* CCK+
569 basket and axo-axonic cells (Freund and Buzsáki, 1996; Soriano et al., 1990). While this study
570 only examined PV-INs after TBI, understanding the effects of CCK+ basket cell inhibition will
571 provide a complete picture of alterations in granule cell perisomatic inhibition. In addition, we
572 did not investigate possible mechanisms of synaptic alterations such as the number of synapses,
573 presynaptic probability of release, or firing activity of presynaptic neurons. Future investigation
574 of the mechanisms of E/I imbalance are crucial to understanding the overall shift in network
575 excitability. Lastly, while both male and female mice were utilized for experiments, we did not
576 explicitly explore sex as an experimental variable in this study. Previously, our laboratory has
577 demonstrated that female and male mice similarly experience higher fEPSP I/O curves seven
578 days after LFPI (citation redacted), however the current study does not explicitly compare sex
579 differences in dentate PV-IN physiology after injury.
580
581 In conclusion, our data show that synaptic input onto dentate PV-INs is altered after injury and is
582 associated with diminished afferent activation of PV-INs driven by network inhibition. Inhibition
583 decreases action potential initiation and suggests that activation of PV-IN-mediated feedforward
584 inhibition onto granule cells in the dentate gyrus is compromised following brain injury. These
585 results demonstrate post-traumatic alterations in inhibitory function that may contribute to

586 dentate network hyperexcitability and may hold therapeutic significance in the future as a
587 specific cellular target for restoring hippocampal dysfunction after TBI.
588
589
590 **References**

591 Armstrong C, Soltesz I (2012) Basket cell dichotomy in microcircuit function. *J Physiol.*
592 **590**:683-94.
593 Butler CR, Boychuk JA, Smith BN (2017) Brain injury-induced synaptic reorganization in hilar
594 inhibitory neurons is differentially suppressed by rapamycin. *eNeuro.* **5**:ENEURO.0134-
595 17.2017.
596 Coulter DA, Carlson GC (2007) Functional regulation of the dentate gyrus by GABA-mediated
597 inhibition. *Prog Brain Res.* **163**:235-43.
598 Diamond JS, Jahr CE (1997) Transporters buffer synaptically released glutamate on a
599 submillisecond time scale. *J Neurosci.* **17**:4672-87.
600 Eisch AJ, Barrot M, Schad CA, Self DW, Nestler EJ (2000) Opiates inhibit neurogenesis in the
601 adult rat hippocampus. *Proc Natl Acad Sci.* **97**:7579-84.
602 Ewell LA, Jones M V. (2010) Frequency-tuned distribution of inhibition in the dentate gyrus. *J*
603 *Neurosci.* **30**:12597-607.
604 Faul F, Erdfelder E, Lang A, Buchner A (2007) G*Power 3.1 manual. *Behavioral Research*
605 *Methods* **39**:175-191.
606 Folweiler KA, Samuel S, Metheny HE, Cohen AS (2018) Diminished dentate gyrus filtering of
607 cortical input leads to enhanced area ca3 excitability after mild traumatic brain injury. *J*
608 *Neurotrauma* **35**:1304-1317.

609 Fredj N Ben, Burrone J (2009) A resting pool of vesicles is responsible for spontaneous vesicle
610 fusion at the synapse. *Nat Neurosci.* **12**:751-8.
611 Freund TF, Buzsáki G (1996) Interneurons of the hippocampus. Hippocampus **6**:347–470.
612 Fuchs EC, Zivkovic AR, Cunningham MO, Middleton S, LeBeau FEN, Bannerman DM, Rozov
613 A, Whittington MA, Traub RD, Rawlins JNP, Monyer H (2007) Recruitment of
614 parvalbumin-positive interneurons determines hippocampal function and associated
615 behavior. *Neuron* **53**:591-604.
616 Gupta A, Elgammal FS, Proddutur A, Shah S, Santhakumar V (2012) Decrease in tonic
617 inhibition contributes to increase in dentate semilunar granule cell excitability after brain
618 injury. *J Neurosci.* **32**:2523–2537.
619 Howard AL, Neu A, Morgan RJ, Echegoyen JC, Soltesz I (2007) Opposing modifications in
620 intrinsic currents and synaptic inputs in post-traumatic mossy cells: evidence for single-cell
621 homeostasis in a hyperexcitable network. *J Neurophysiol* **97**:2394–409.
622 Hu H, Gan J, Jonas P (2014) Fast-spiking, parvalbumin+ GABAergic interneurons: From
623 cellular design to microcircuit function. *Science* **345**:1255263–1255263.
624 Hunt RF, Scheff SW, Smith BN (2011) Synaptic reorganization of inhibitory hilar interneuron
625 circuitry after traumatic brain injury in mice. *J Neurosci.* **31**:6880–6890.
626 Kawaguchi Y, Kubota Y (1997) GABAergic cell subtypes and their synaptic connections in rat
627 frontal cortex. *Cereb Cortex* **7**:476–86.
628 Kraushaar U, Jonas P (2000) Efficacy and stability of quantal GABA release at a hippocampal
629 interneuron-principal neuron synapse. *J Neurosci.* **20**:5594-607.
630 Lim MM, Elkind J, Xiong G, Galante R, Zhu J, Zhang L, Lian J, Rodin J, Kuzma NN, Pack AI,
631 Cohen AS (2013) Dietary therapy mitigates persistent wake deficits caused by mild

traumatic brain injury. *Sci Transl Med.* **5**:215ra173.

Lowenstein DH, Thomas MJ, Smith DH, McIntosh TK (1992) Selective vulnerability of dentate hilar neurons following traumatic brain injury: a potential mechanistic link between head trauma and disorders of the hippocampus. *J Neurosci* **12**:4846–4853.

Magee JC, Cook EP (2000) Somatic EPSP amplitude is independent of synapse location in hippocampal pyramidal neurons. *Nat Neurosci.* **3**:895-903.

Mathew SS, Pozzo-Miller L, Hablitz JJ (2008) Kainate modulates presynaptic GABA release from two vesicle pools. *J Neurosci* **28**:725–731.

Mody I, Pearce RA (2004) Diversity of inhibitory neurotransmission through GABA(A) receptors. *Trends Neurosci.* **27**:569-75.

Mouton PR (2002) Principles and Practices of Unbiased Stereology: An Introduction for Bioscientists. Baltimore, Maryland: Johns Hopkins University Press.

Nichols J, Bjorklund GR, Newbern J, Anderson T (2018) Parvalbumin fast-spiking interneurons are selectively altered by paediatric traumatic brain injury. *J Physiol* **596**:1277–1293.

Nitz D, Mcnaughton B (2004) Interneurons during exploration of novel environments differential modulation of CA1 and dentate gyrus differential modulation of CA1 and dentate gyrus interneurons during exploration of novel environments. *J Neurophysiol* **91**:863–872.

Ross ST, Soltesz I (2000) Selective depolarization of interneurons in the early posttraumatic dentate gyrus: involvement of the Na(+)/K(+)-ATPase. *J Neurophysiol* **83**:2916–2930.

Rossi D, Hamann M (1998) Spillover-mediated transmission at inhibitory synapses promoted by high affinity alpha6 subunit GABA(A) receptors and glomerular geometry. *Neuron* **20**:783-95.

Santhakumar V, Bender R, Frotscher M, Ross ST, Hollrigel GS, Toth Z, Soltesz I (2000)

655 Granule cell hyperexcitability in the early post-traumatic rat dentate gyrus: the “irritable
656 mossy cell” hypothesis. *J Physiol* **524 Pt 1**:117–34.
657 Santhakumar V, Ratzliff ADH, Jeng J, Toth Z, Soltesz I (2001) Long-term hyperexcitability in
658 the hippocampus after experimental head trauma. *Ann Neurol* **50**:708–717.
659 Sara Y, Virmani T, Deák F, Liu X, Kavalali ET (2005) An isolated pool of vesicles recycles at
660 rest and drives spontaneous neurotransmission. *Neuron* **45**:563-73.
661 Soltesz I, Smetters DK, Mody I (1995) Tonic inhibition originates from synapses close to the
662 soma. *Neuron* **14**:1273–1283.
663 Soriano E, Nitsch R, Frotscher M (1990) Axo-axonic chandelier cells in the rat fascia dentata:
664 Golgi-electron microscopy and immunocytochemical studies. *J Comp Neurol.* **293**:1-25.
665 Stell BM, Mody I (2002) Receptors with different affinities mediate phasic and tonic GABA(A)
666 conductances in hippocampal neurons. *J. Neurosci.* **22**:RC223.
667 Szabo GG, Du X, Oijala M, Varga C, Parent JM, Soltesz I (2017) Extended interneuronal
668 network of the dentate gyrus. *Cell Rep.* **20**:1262-1268.
669 Toth Z, Hollrigel GS, Gorcs T, Soltesz I (1997) Instantaneous perturbation of dentate
670 interneuronal networks by a pressure wave-transient delivered to the neocortex. *J Neurosci*
671 **17**:8106–17.
672 Van der Zee CEEM, Rashid K, Le K, Moore KA, Stanisz J, Diamond J, Racine RJ, Fahnestock
673 M (1995) Intraventricular administration of antibodies to nerve growth factor retards
674 kindling and blocks mossy fiber sprouting in adult rats. *J Neurosci.* **15**:5316-23.
675 West MJ, Slomianka L, Gundersen HJG (1991) Unbiased stereological estimation of the total
676 number of neurons in the subdivisions of the rat hippocampus using the optical fractionator.
677 *Anat Rec.* **231**:482-97.

678 Williams SR, Mitchell SJ (2008) Direct measurement of somatic voltage clamp errors in central
679 neurons. *Nat Neurosci.* **11**:790-8.
680 Witgen BM, Lifshitz J, Smith ML, Schwarzbach E, Liang SL, Grady MS, Cohen AS (2005)
681 Regional hippocampal alteration associated with cognitive deficit following experimental
682 brain injury: A systems, network and cellular evaluation. *Neuroscience* **133**:1–15.
683 Zhang BL, Fan YS, Wang JW, Zhou ZW, Wu YG, Yang MC, Sun DD, Zhang JN (2018)
684 Cognitive impairment after traumatic brain injury is associated with reduced long-term
685 depression of excitatory postsynaptic potential in the rat hippocampal dentate gyrus. *Neural*
686 *Regen Res.* **13**:1753-1758.s
687 Zhang W, Buckmaster PS (2009) Dysfunction of the dentate basket cell circuit in a rat model of
688 temporal lobe epilepsy. *J Neurosci.* **29**:7846-56.
689
690
691
692
693
694
695
696
697
698
699
700

Figures

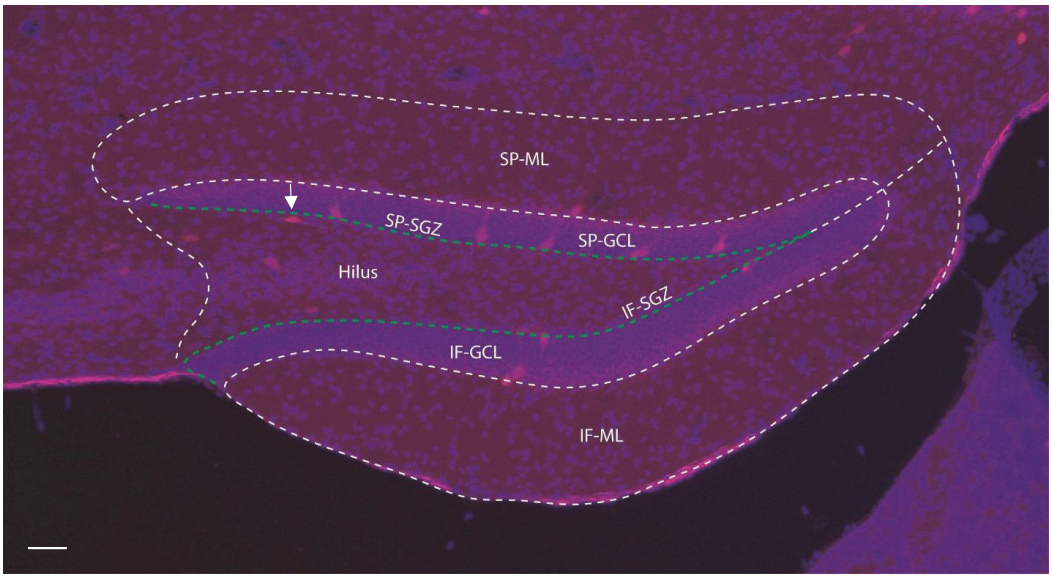

Figure 1. Anatomical layers of the dentate gyrus used to determine PV+ cell location for counting. Overlay of Hoechst staining (blue) of all cells in the slice was used to identify the

718 anatomical structure and cellular layer boundaries (dotted white line) of the dentate gyrus when
719 counting tdTomato-expressing (red) parvalbumin-positive cells. Cell anatomical location was
720 divided by both dentate blade—suprapyramidal (SP) or infrapyramidal (IP)—and cellular layer,
721 including molecular layer (ML), granule cell layer (GCL), subgranular zone (SGZ), and hilus.
722 TdTomato-expressing cells in the hilus but within one soma length (20-30 µm) of the granule
723 cell layer were considered in the subgranular zone (white arrow). Lower left: scale bar, 50 µm.

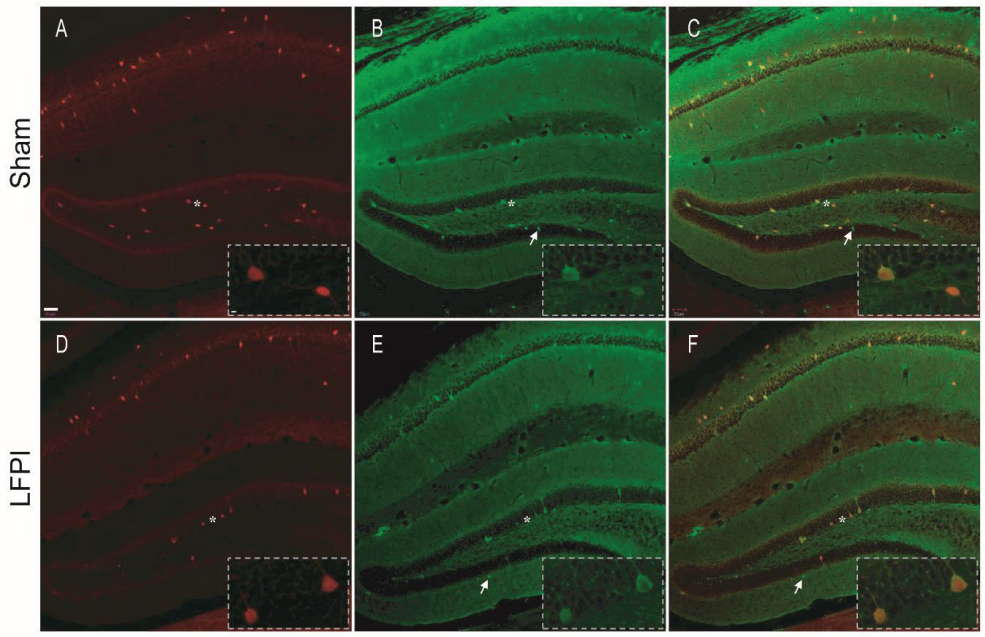

724
725 **Figure 2**. Immunofluorescent staining to confirm dentate parvalbumin expression in tdTomato-
726 positive cells in both sham (top row) and LFPI (bottom row) animals seven days after surgery.
727 A) and D) Transgenic expression of tdTomato fluorescence (red) in parvalbumin-positive cells
728 expressing Cre-recombinase. B) and E) Immunofluorescent staining of parvalbumin-expressing
729 cells (green). C) and F) Co-localization of td-Tomato and immunofluorescence (inset)

730 demonstrates that most td-Tomato-expressing cells are parvalbumin-positive. Asterisk indicates
731 the location of the inset. A small portion of parvalbumin-expressing cells (green) did not express
732 td-Tomato (white arrows).
733

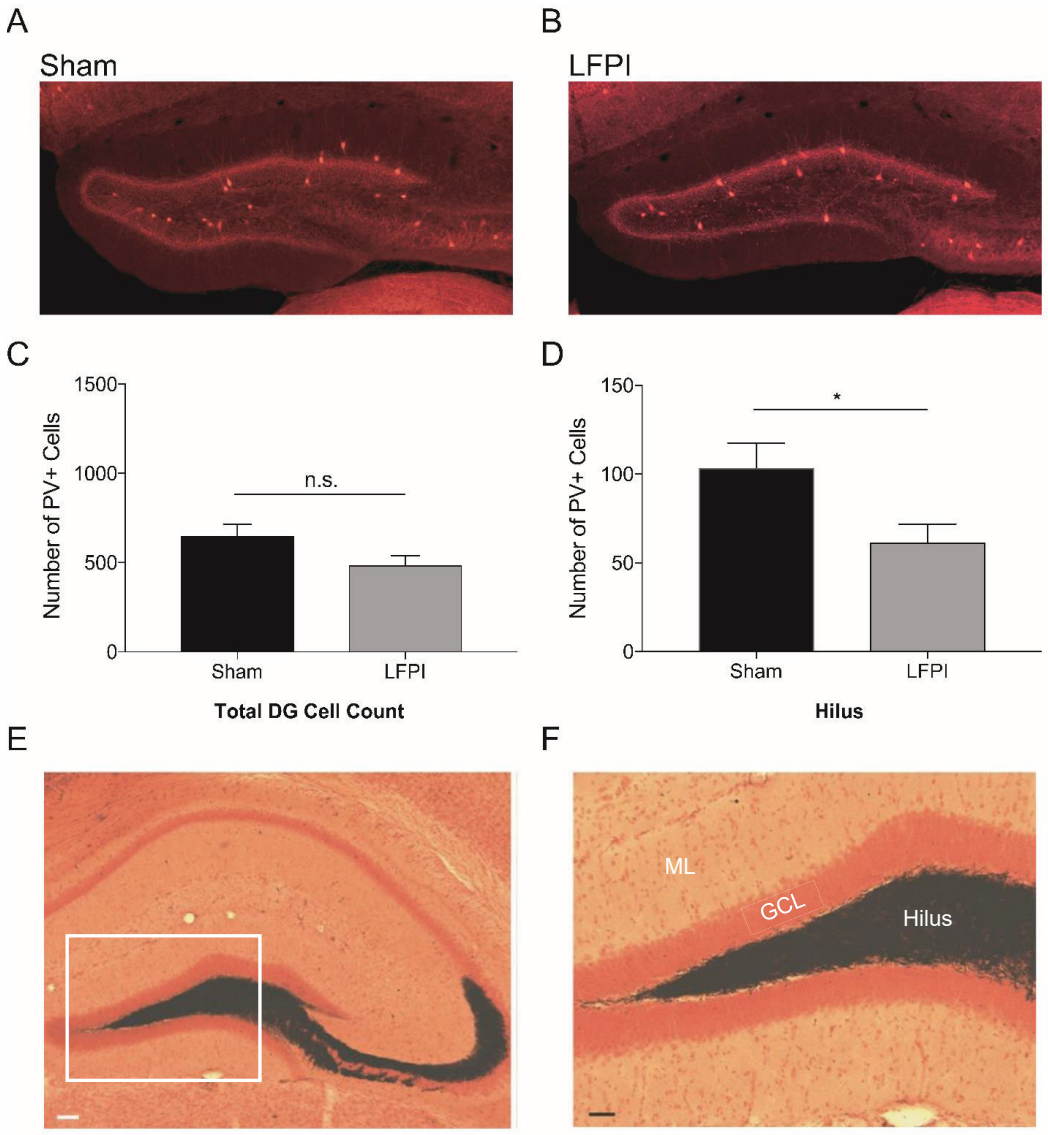

734
735 **Figure 3.** PV-IN cell loss in the dentate hilus occurs one week after mild LFPI. Parvalbumin-
736 positive (PV+) inhibitory interneurons expressing the fluorescent marker tdTomato in the dentate
737 gyrus one week after A) sham surgery or B) LFPI. C) Total number of PV+ cell bodies in the
738 dentate gyrus (DG) are not significantly different between sham and LFPI. D) The hilus

739 experiences a significant loss of PV+ interneurons. n.s., non-significant; * $p < 0.05$. E) Timm
740 staining of granule cell mossy fiber projections (black) into the hilus and area CA3 in an LFPI
741 animal seven days after injury, scale bar 50 µm Inset (white box) magnified in F) demonstrates
742 no Timm stained fibers are present in the inner molecular layer (ML) adjacent to the granule cell
743 layer (GCL) where mossy fiber sprouting would occurscale bar, 25 µm.

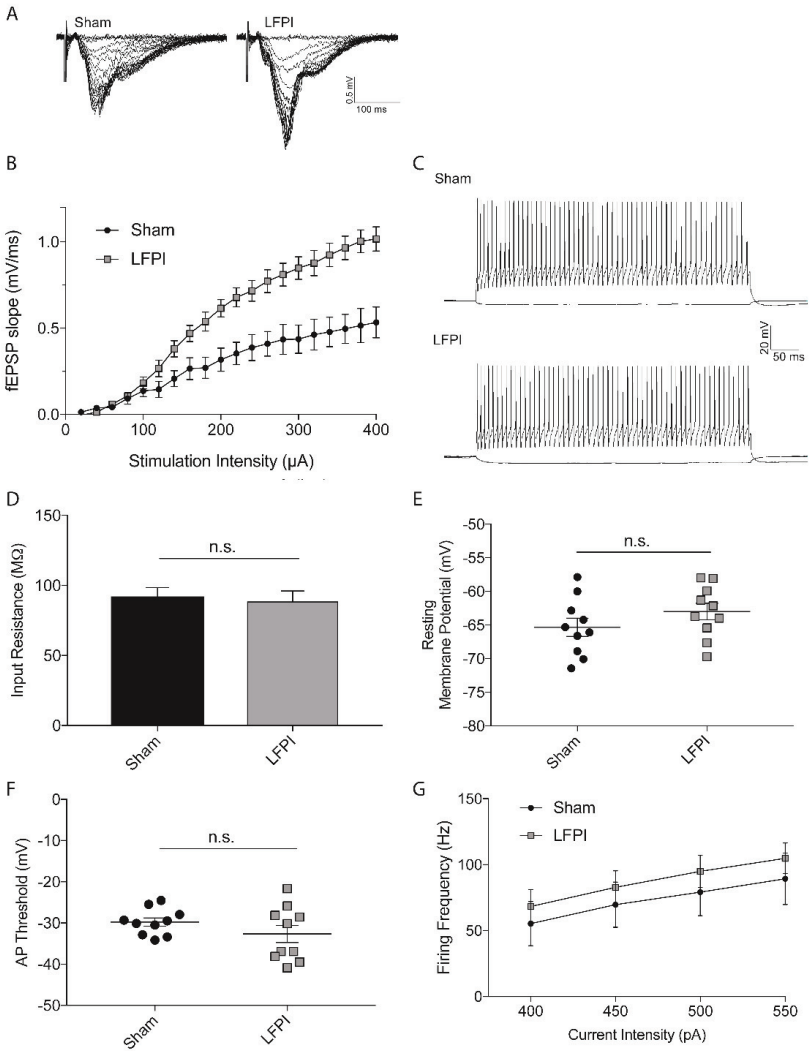

744
745
746

Figure 4. PV-IN intrinsic membrane excitability remains intact after LFPI. A) Field excitatory postsynaptic potentials (fEPSPs) recorded from dentate molecular layer suggests dentate network hyperexcitability in transgenic PV-Tomato mouse line in response to perforant path electrical stimulation as demonstrated by B) significantly larger fEPSP slopes in LFPI mice than sham mice within the stimulation intensity range of 20-400 μA, 20 μA increments, 100 μs duration. C) Example membrane voltage traces from sham (top trace) and LFPI (bottom trace) PV-INs in response to -50 pA and +100 pA current injections. Passive membrane properties of PV-INs are unchanged by injury as exemplified by D) membrane input resistance and E) resting membrane potential. Active firing properties also show no significant difference between sham (black points) and injured (gray points) on F) action potential threshold and G) PV-IN firing frequency in response to increasing depolarizing current injections.

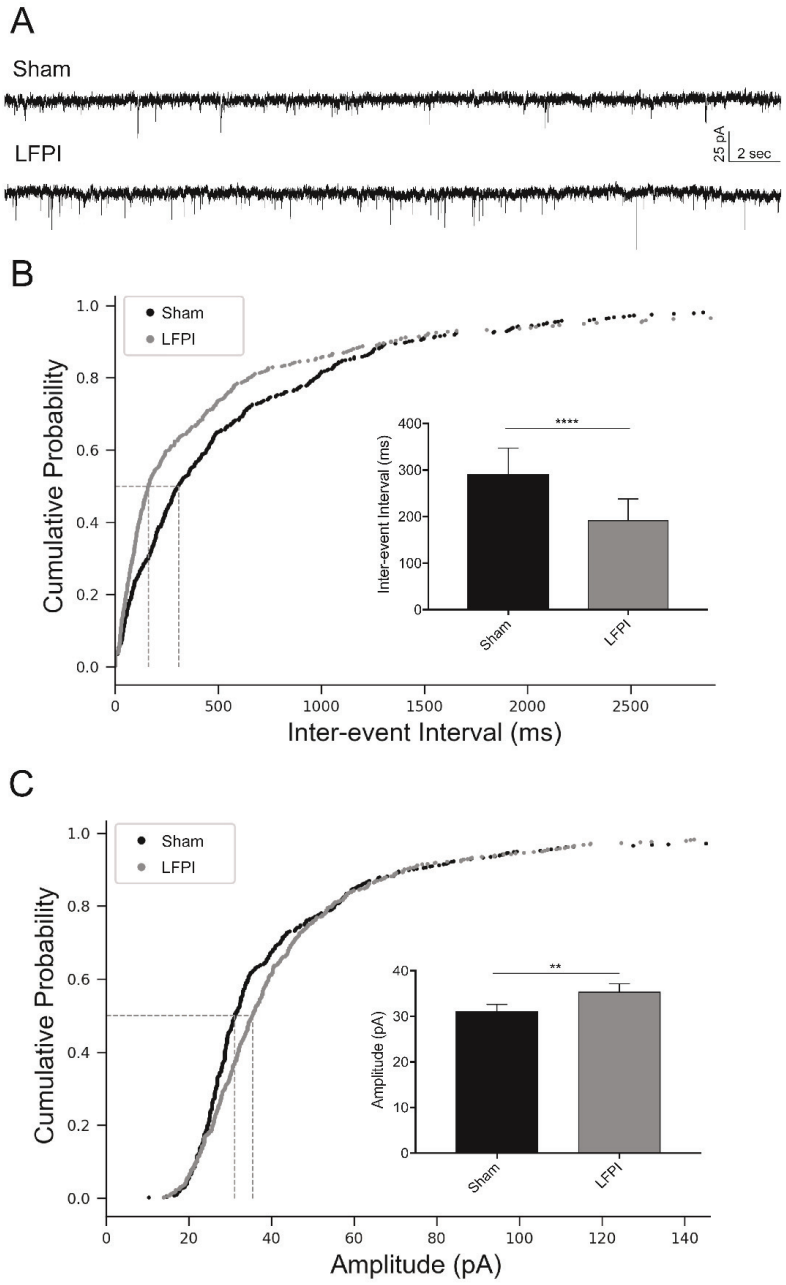

Figure 5. PV-IN mEPSCs are larger and more frequent after LFPI. A) Representative traces of voltage-clamp recordings from sham (top trace) and LFPI (bottom trace) PV-IN cells in the presence of 30 μM bicuculline methiodide and 0.4 μM tetrodotoxin to block presynaptic action

potential-dependent synaptic transmission. Cumulative probability plots of B) mEPSC inter-event interval and C) event amplitude from sham PV-INs (black) and LFPI PV-INs (gray). Vertical dashed lines indicate the median of the distribution at probability, p = 0.5. Insets: bar graphs of the median and 95% confidence intervals of B) mEPSC inter-event interval and C) mEPSC amplitude in sham (black) and LFPI (gray) PV-INs. ***, p < 0.001, **, p < 0.01

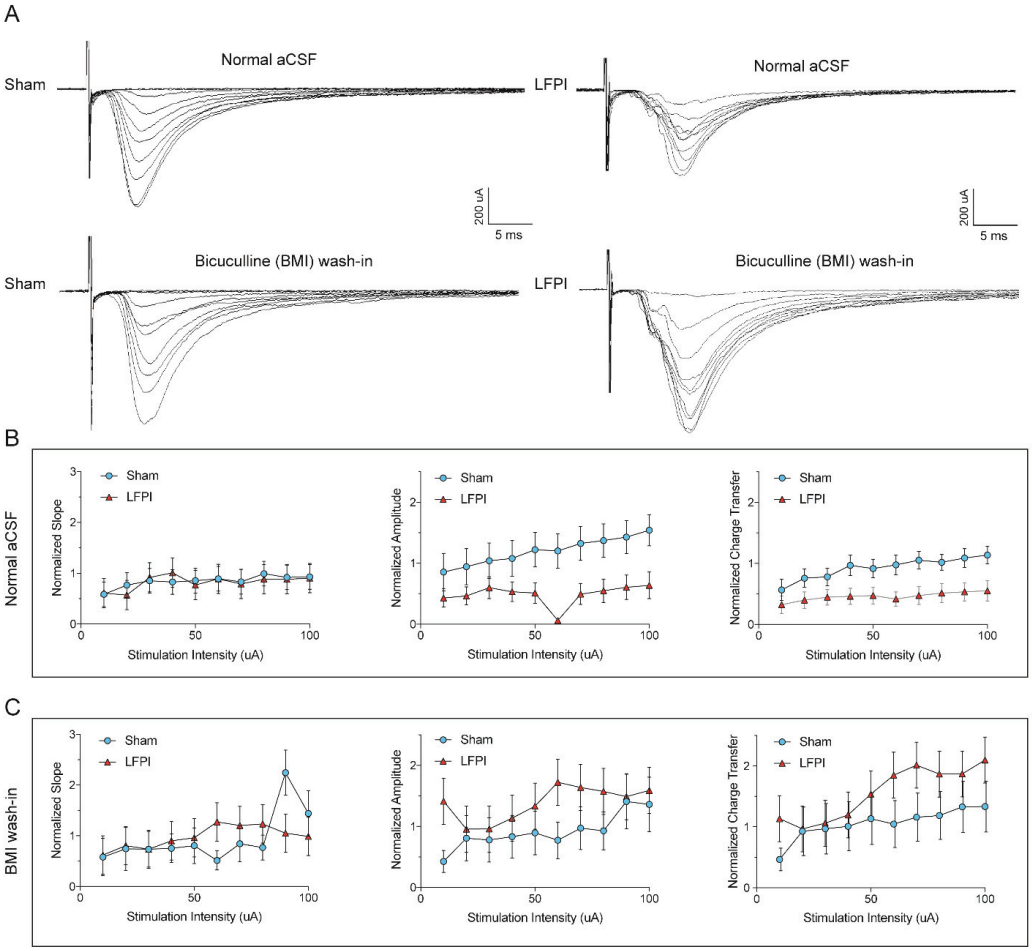

Figure 6. Decreased perforant path evoked EPSCs onto PV-INs after LFPI. A) Representative traces of perforant path evoked EPSCs onto PV-INs from sham (top left), LFPI (top right), and

771 the same sham (bottom left) and LFPI (bottom right) cells with the addition of bicuculline
772 methiodide (BMI). Evoked EPSCs were normalized to the fiber volley (FV) amplitude of the
773 extracellular field response of that brain slice. The FV-normalized B *left*) slope, B *middle*)
774 amplitude, and B *right*) charge transfer of eEPSCs in sham (blue) and LFPI (red) PV-INs. FV-
775 normalized C *left*) slope, C *middle*) amplitude, and C *right*) charge transfer of eEPSCs after BMI
776 wash-in.

777
778
779

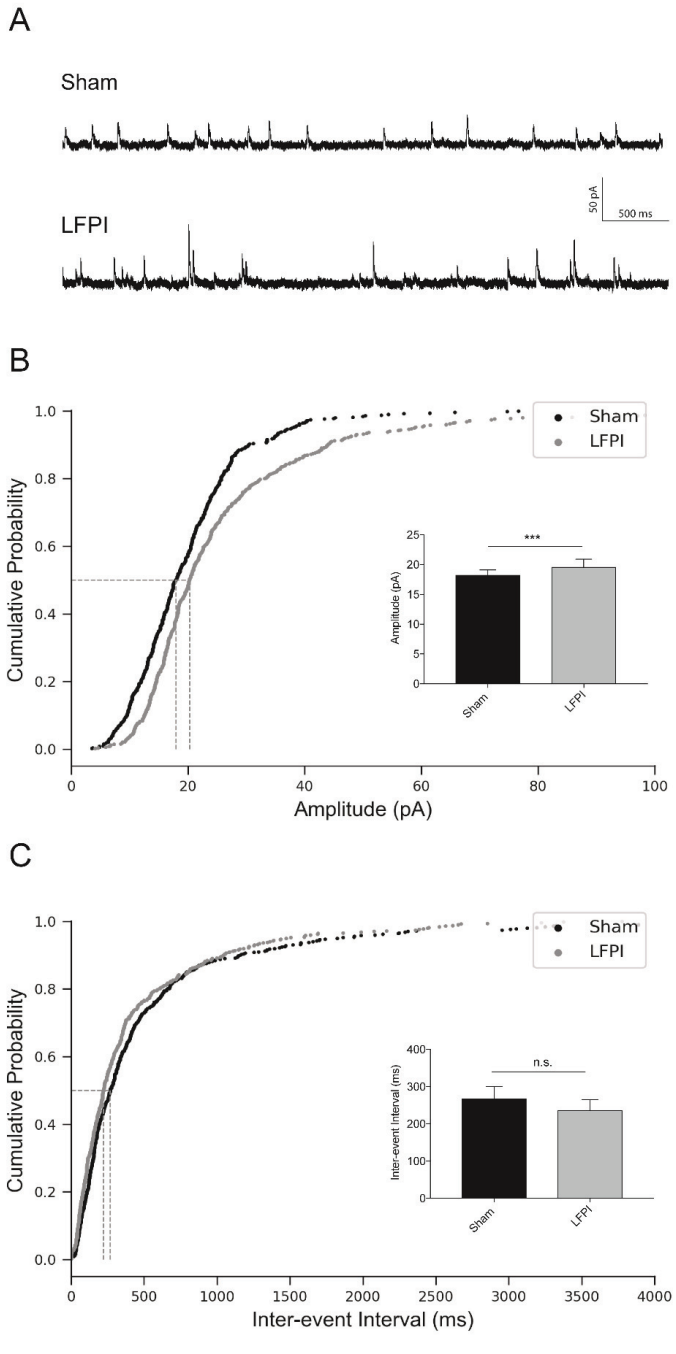

780

781 **Figure 7.** Increase in PV-IN miniature IPSC amplitude after LFPI. A) Representative traces of
782 voltage-clamp recordings at 0 mV from sham (top trace) and LFPI (bottom trace) PV-IN cells in
783 the presence of glutamatergic blockers, APV and CNQX, and 0.4 μM TTX to isolate action-
784 potential-independent synaptic transmission. Cumulative probability plots of B) mIPSC
785 amplitude, C) inter-event interval from sham PV-INs (black) and LFPI PV-INs (gray). Vertical
786 dashed lines indicate the median of the distribution at probability, $p = 0.5$. Insets: bar graphs of
787 the median and 95% confidence intervals for respective event measurements in sham (black) and
788 LFPI (gray). n.s., no significance, ***, $p < 0.001$.
789
790
791
792
793
794
795
796
797
798
799

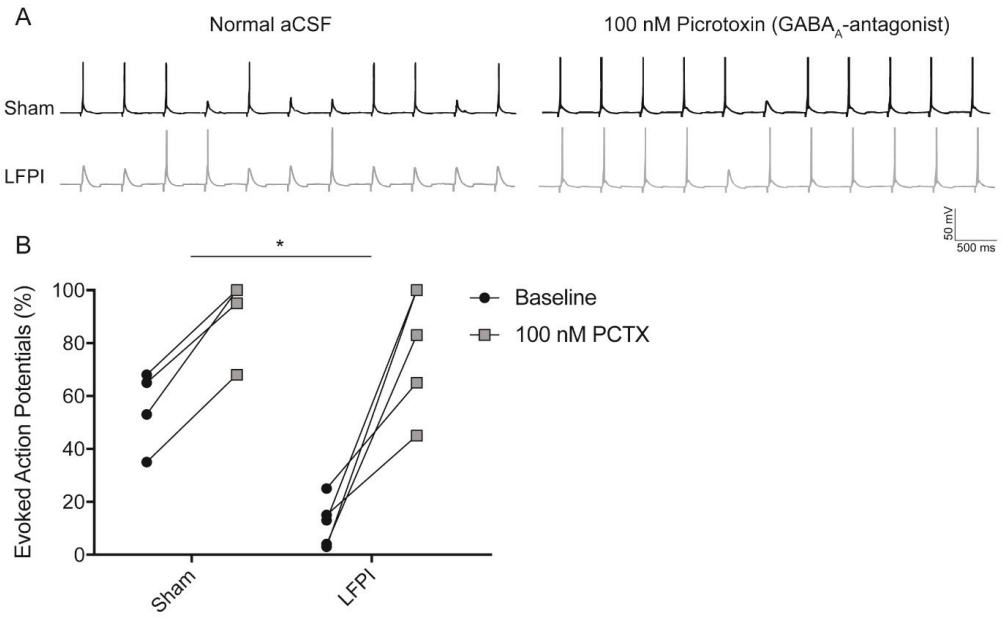

Figure 8. Feed-forward activation of PV-INs is diminished by increased network inhibitory input. A) Minimal electrical stimulation evoked voltage responses for individual cells in sham (top left trace) and LFPI (bottom left trace) slices during whole-cell current-clamp recordings with a holding potential of -65 mV in normal aCSF solution (left) and with bath application of 100 nM picrotoxin (Sham, right top trace; LFPI, right bottom trace) while recording the same cell with 12 second inter-stimulus intervals (intervals shorted to 500 ms in figure). B) Percentage of evoked action potentials elicited in response to a sequence of 20 stimulations (i.e., 10 evoked APs in 20 stimulations = 50%) at baseline in normal aCSF perfusion solution and after bath application of picrotoxin. Percent differences in evoked responses for sham (mean ± SEM): 34.8% ± 3.1 (n = 5 cells), and for LFPI (mean ± SEM): 66.6% ± 13.31 (n = 5 cells). *, p = 0.0008, Welch's unpaired t-test.

816

817 **Tables**

818

Experiment	Sham		LFPI	
	Male (n)	Female (n)	Male (n)	Female (n)
Immunostaining	3	0	4	0
Cell Counts	6	2	4	5
Timm Staining	10	0	10	0
Field EPSPs	4	2	3	3
Intrinsic Properties	5	5	4	6
Miniature EPSCs	4	3	3	3
Evoked EPSCs	7	5	8	3
Miniature IPSCs	2	4	5	2
Evoked APs	3	2	3	2

819

820 **Table 1. Male and female mice per group used in each experiment.** For each experiment (left
821 column) the sample size of male and female mice in sham and LFPI groups. Abbreviations: n,
822 sample size; EPSCs, excitatory postsynaptic currents; IPSCs, inhibitory postsynaptic currents;
823 APs, action potentials.

824

	Experiment	Data Structure	Type of Test	Test Statistic	P-value
Immunostaining					

1a	Td-Tomato/PV-immunostain colocalization	Normal (SW & DP)	Two-tailed unpaired t-test	t = 0.065 df = 4.42	p = 0.95
1b	PV-immunostained cells only	Normal (SW & DP)	Two-tailed unpaired t-test	t = 0.721 df = 5	p = 0.47
1c	TdTomato cells only	Normal (SW & DP)	Two-tailed unpaired t-test	t = 0.774 df = 5	p = 0.56
Cell Counts					
2a	Total DG	Normal (SW & DP)	Two-tailed unpaired t-test	t = 1.971 df = 15	p = 0.07
2b	Hilus	Normal (SW & DP)	Two-tailed unpaired t-test	t = 2.431 df = 15	p = 0.03
2c	Subgranular Zone	Normal (SW & DP)	Two-tailed unpaired t-test	t = 1.579 df = 15	p = 0.14
2d	Granule Cell Layer	Normal (SW)	Two-tailed unpaired t-test	t = 0.6157 df = 15	p = 0.55
2e	Molecular Layer	Normal (SW & DP)	Two-tailed unpaired t-test	t = 0.9811 df = 15	p = 0.34
2f	Suprapyramidal Blade	Normal (SW & DP)	Two-tailed unpaired t-test	t = 2.048 df = 15	p = 0.06
2g	Infrapyramidal Blade	Normal (SW & DP)	Two-tailed unpaired t-test	t = 1.117 df = 15	p = 0.28

2f	Septotemporal	Normal (DP)	Two-way ANOVA	F (1,87) = 0.87	p = 0.35
Intrinsic Properties					
3a	Field EPSPs	Normal (SW & DP)	Repeated measures ANOVA	F(19,190) = 14.34	p < 0.0001
3b	Input Resistance	Normal (DP)	Two-tailed unpaired t-test	t = 0.3717 df = 18	p = 0.71
3c	Resting Membrane Potential	Normal (SW & DP)	Two-tailed unpaired t-test	t = 1.279 df = 18	p = 0.21
3d	AP Threshold	Normal (SW)	Two-tailed unpaired t-test	t = 1.244 df = 18	p = 0.23
3e	AP Firing Frequency	Normal (SW)	Repeated measures ANOVA	F (1, 13) = 0.422	p = 0.53
3f	AP half-width	Normal (SW)	Two-tailed unpaired t-test	t = 0.612 df = 14	p = 0.55
Miniature EPSCs					
4a	Inter-event Interval	Non-normal (SW & DP)	Kolmogorov-Smirnov test	D = 0.162	p < 0.0001
4b	Amplitude	Non-normal (SW & DP)	Kolmogorov-Smirnov test	D = 0.113	p = 0.006
4c	Rise Tau	Non-normal (SW & DP)	Kolmogorov-Smirnov test	D = 0.104	p = 0.004

4d	Decay Tau	Non-normal (SW & DP)	Kolmogorov-Smirnov test	D = 0.072	p = 0.20
Evoked EPSCs					
5a	Slope	Normal (SW & DP)	Two-way ANOVA	F (1, 13) = 0.1825	p = 0.68
5b	Amplitude	Normal (SW & DP)	Two-way ANOVA	F (1, 22) = 4.715	p = 0.04
5c	Charge Transfer	Normal (SW & DP)	Two-way ANOVA	F (1, 21) = 5.426	p = 0.03
5d	Slope (BMI wash-in)	Normal (SW & DP)	Two-way ANOVA	F (1, 10) = 0.005518	p = 0.94
5e	Amplitude (BMI wash-in)	Normal (SW & DP)	Two-way ANOVA	F (1, 10) = 0.8552	p = 0.38
5f	Charge Transfer (BMI wash-in)	Normal (SW & DP)	Two-way ANOVA	F (1, 10) = 0.9528	p = 0.35
Miniature IPSCs					
6a	Amplitude	Non-normal (SW & DP)	Kolmogorov-Smirnov test	D = 0.134	p = 0.0003
6b	Rise Tau	Non-normal (SW & DP)	Kolmogorov-Smirnov test	D = 0.126	p = 0.008
6c	Inter-event Interval	Non-normal (SW & DP)	Kolmogorov-Smirnov test	D = 0.064	p = 0.25

6d	Decay Tau	Non-normal (SW & DP)	Kolmogorov-Smirnov test	D = 0.038	p = 0.86
Evoked APs					
7a	Resting Membrane Potential	Normal (SW)	Welch's unpaired t-test	t = 0.9494 df = 8	p = 0.37
7b	Whole-cell Capacitance	Normal (SW)	Welch's unpaired t-test	t = 0.4834 df = 8	p = 0.64
7c	Evoked APs (Normal aCSF)	Normal (SW)	Welch's unpaired t-test	t = 9.084 df = 4	p = 0.0008
7d	Evoked APs (Sham pre- and post-PCTX)	Normal (SW)	Paired t-test	t = 11.27, df = 4	p = 0.0004
7e	Evoked APs (LFPI pre- and post-PCTX)	Normal (SW)	Paired t-test	t = 5.119 df = 4	p = 0.0034
9f	Evoked APs (100nm PCTX)	Normal (SW)	Welch's unpaired t-test	t = 1.138 df = 6	p = 0.29

Table 2. Statistical analysis of experimental results. For each experiment (second column), the statistical results included the structure of the data distribution as determined by Shapiro-Wilk (SW) or D'Agostino-Pearson (DP) normality tests (third column), the statistical test used, the test statistic and degrees of freedom (df), and the p-value. P-values greater than 0.05 are rounded up to two decimal places. Abbreviations: DG, dentate gyrus; EPSCs, excitatory postsynaptic

currents; IPSCs, inhibitory postsynaptic currents; APs, action potentials; aCSF, artificial cerebral spinal fluid; PCTX, picrotoxin.